 CMC, vol.18, no.2, pp.155-182, 2010

Buckling and Postbuckling Behavior of Functionally Graded Nanotube-Reinforced Composite Plates in Thermal Environments

Hui-Shen Shen[1,2] **and Zheng Hong Zhu**[3]

Abstract: This paper investigates the buckling and postbuckling of simply supported, nanocomposite plates with functionally graded nanotube reinforcements subjected to uniaxial compression in thermal environments. The nanocomposite plates are assumed to be functionally graded in the thickness direction using single-walled carbon nanotubes (SWCNTs) serving as reinforcements and the plates' effective material properties are estimated through a micromechanical model. The higher order shear deformation plate theory with a von Kármán-type of kinematic nonlinearity is used to model the composite plates and a two-step perturbation technique is performed to determine the buckling loads and postbuckling equilibrium paths. Numerical results for perfect and imperfect, geometrically mid-plane symmetric functionally graded carbon nanotube reinforced composite (FG-CNTRC) plates are obtained under different sets of thermal environmental conditions. The results for uniformly distributed CNTRC plate, which is a special case in the present study, are compared with those of the FG-CNTRC plate. The results show that the buckling loads as well as postbuckling strength of the plate can be significantly increased as a result of a functionally graded nanotube reinforcement. The results reveal that the carbon nanotube volume fraction has a significant effect on the buckling load and postbuckling behavior of CNTRC plates.

Keywords: Nanocomposites; Functionally graded materials; Plates; Buckling; Postbuckling

[1] School of Ocean and Civil Engineering & State Key Laboratory of Ocean Engineering, Shanghai Jiao Tong University, Shanghai 200030, People's Republic of China

[2] Corresponding author. E-mail address: hsshen@mail.sjtu.edu.cn

[3] Department of Earth and Space Science and Engineering, York University, 4700 Keele Street, Toronto, Ontario, Canada M3J 1P3

1 Introduction

Achieving maximum buckling and postbuckling strength is one of the critical issues in the design of thin-walled and lightweight structures. Carbon nanotubes (CNTs) are regarded as one of the most promising reinforcement materials for the next generation of high-performance structural and multifunctional composites [Endo et al. (2004)]. These nanoscale tubes have outstanding mechanical and thermal properties. Their unique properties combined with their high aspect ratio (i.e., in the thousands) and low density, have brought about extensive researches concerned with reinforcing the advanced composites using CNTs [Seidel and Lagoudas (2006); Esawi and Farag (2007); Li et al. (2007); McClory et al. (2009); Thostenson et al. (2010)]. The carbon nanotube-reinforced composites (CNTRCs) offer significant potential of increased strength and stiffness by homogeneous dispersion of a small percentage of CTNs (2∼5% by weight) into a matrix [Griebel and Hamaekers (2004); Fidelus et al. (2005); McClory et al. (2009); Song and Youn (2006); Han and Elliott (2007); Zhu et al. (2007); Tsai et al. (2010)]. For instance, Wuite and Adali (2005) found that the stiffness of CNTRC beams can be improved significantly by the homogeneous dispersion of a small percentage of CNTs. Vodenitcharova and Zhang (2006) studied the pure bending and bending-induced local buckling of CNTRC beams. Unfortunately, the reinforcement by the homogeneous dispersion of CNTs can achieve a moderate improvement of the mechanical properties of CNTRC only [Schadler et al. (1998); Qian et al. (2000)]. Formica et al. (2010) further pointed out that the improvement achieves a maximum when the CNTs are uniformly aligned with the loading direction when investigating the vibration behavior of CNTRC plates by an equivalent continuum model that is based on the Mori–Tanaka approach.

Functionally graded materials (FGMs) are a new generation of composite materials in which the microstructural details are spatially varied through nonuniform distribution of the reinforcement phase. Two kinds of FGMs are designed to improve mechanical behavior of plate/shell structures. One is functionally graded unidirectional fibers reinforced composites [Birman (1995); Feldman and Aboudi (1997); Yas and Aragh (2010)]. Another one, like functionally graded ceramic-metal materials, is functionally graded particles reinforced composites [Yang et al. (2006); Woo et al. (2005); Shen (2005)]. The concept of FGM can be utilized for the CNTRC by non-homogeneous distribution of CNTs into the composite plates with a specific gradient so that the buckling behavior of CNTRC plates can be improved. Shen (2009b) suggested that the nonlinear bending behavior can be considerably improved through the use of a functionally graded distribution of CNTs in the matrix. The effect of CNT volume fraction on the thermal postbuckling behavior of functionally graded CNTRC plates was reported by Shen and Zhang (2010). They

found that in some cases the CNTRC plate with intermediate CNT volume fraction does not have intermediate buckling temperature and initial thermal postbuckling strength. Moreover, Ke et al. (2010) investigated the nonlinear free vibration of functionally graded CNTRC Timoshenko beams. They found that both linear and nonlinear frequencies of functionally graded CNTRC beam with symmetrical distribution of CNTs are higher than those of beams with uniform or unsymmetrical distribution of CNTs.

The present work focuses attention on the postbuckling analysis of CNTRC plates subject to uniaxial compression in thermal environments. Unlike the carbon fiber reinforced composites, the CNTRCs usually have a lower volume fraction of CNTs due to the fact their mechanical properties will deteriorate if the volume fraction increases certain limit [Meguid and Sun (2004)]. One of the problems is how to increase the buckling load and postbuckling strength of CNTRC plates under such a low nanotube volume fraction. It has been address in the current paper by a novel functionally graded reinforcing scheme in the thickness direction. It is assumed that the properties of SWCNTs are size and temperature dependent and can be derived via molecular dynamics (MD) simulations. The descriptions of properties and the reinforcing functional gradients of SWCNTs provide the basis for the development of equivalent material properties of functionally graded CNTRCs (FG-CNTRC) through a micromechanical model, in which the CNT efficiency parameter is estimated by matching the elastic modulus of CNTRCs predicted by MD simulations with the extended rule of mixture. These underlying properties are subsequently used in analysis to enhance postbuckling performance of CNTRCs plates. In the current approach, the FG-CNTRCs plate is modeled by a higher order shear deformation plate theory with a von Kármán-type of kinematic nonlinearity and including thermal effect. The effect of initial geometric imperfection of the plate is also considered in the current model.

2 Multi-scale model for functionally graded CNTRC plates

It has been reported that there is no bifurcation buckling for simply supported functionally graded plates subjected to uniaxial or biaxial compression, except the plate is mid-plane symmetric [Shen (2005); Navazi and Haddadpour (2008)]. For this reason, we consider a rectangular CNTRC plate which consists of two layers made of functionally graded materials and is mid-plane symmetric, as shown in Fig. 1. It is worth noting that for fully clamped FG-CNTRC plates the buckling loads do exist and the assumption of mid-plane symmetric structure is unnecessary. The length, width and total thickness of the CNTRC plate are a, b and t. As usual, the coordinate system has its origin at the corner of the plate on the middle plane. The X-axis is defined along the plate's longitudinal edge while the Z-axis being perpendicular

to the mid-plane. Let $\bar{U}$, $\bar{V}$ and $\bar{W}$ be the displacement components of the mid-plane in X, Y, and Z axes and $\bar{\Psi}_x$ and $\bar{\Psi}_y$ be the rotations of the mid-plane normal about Y and X axes, respectively. The plate is assumed to be geometrically imperfect initially, and is subjected to a compressive edge load in the X direction. Denoting the initial geometric imperfection by $\bar{W}^*(X,Y)$ and let $\bar{F}(X,Y)$ be the stress function for the stress resultants defined by $\bar{N}_x = \bar{F}_{,YY}$, $\bar{N}_y = \bar{F}_{,XX}$ and $\bar{N}_{xy} = -\bar{F}_{,XY}$, where the comma is partial differentiation with respect to the corresponding coordinates.

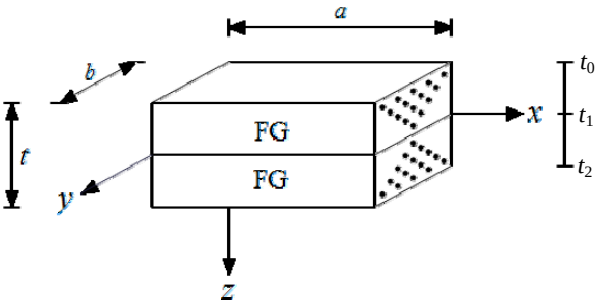

Figure 1: Configuration of a functionally graded carbon nanotube-reinforced composite plate.

For functionally graded fibers reinforced composite plates, layerwise approaches are usually proposed to trace the local variations in each layer more accurately. Zigzag theories have the benefits of less computational times of the layerwise theories. Carrera (2003) has reviewed the history of the zigzag theories of the multilayered plates and shells, and three independent ways of introducing zigzag theories were singled out. These theories describe a piecewise continuous displacement field in the thickness direction of the plate and incorporate the interlaminar continuity of the transverse stresses at each layer interface. On the other hand, Reddy (1984a) developed a simple higher order shear deformation plate theory. This theory assumes that the transverse shear strains are parabolically distributed across the plate thickness. As has been shown [Reddy (2004b)] this theory can accurately predict the global structural responses (deflection, buckling and vibration) of the laminated plates. The advantages of this theory over the first order shear deformation theory are that the number of independent unknowns ($\bar{U}$, $\bar{V}$, $\bar{W}$, $\bar{\Psi}_x$ and $\bar{\Psi}_y$) is the same as in the first order shear deformation theory without the need for shear correction factors. Based on Reddy's higher order shear deformation theory with a von Kármán-type of kinematic nonlinearity and including thermal effect, the governing differential equations for an FG-CNTRC plate can be derived in terms of a stress function$\bar{F}$, two rotations $\bar{\Psi}_x$ and $\bar{\Psi}_y$, and a transverse displacement $\bar{W}$, along

with the initial geometric imperfection $\bar{W}^*$, such that

$$\tilde{L}_{11}(\bar{W})-\tilde{L}_{12}(\bar{\Psi}_x)-\tilde{L}_{13}(\bar{\Psi}_y)+\tilde{L}_{14}(\bar{F})-\tilde{L}_{15}(\bar{N}^T)-\tilde{L}_{16}(\bar{M}^T)=\tilde{L}(\bar{W}+\bar{W}^*,\bar{F}) \quad (1)$$

$$\tilde{L}_{21}(\bar{F})+\tilde{L}_{22}(\bar{\Psi}_x)+\tilde{L}_{23}(\bar{\Psi}_y)-\tilde{L}_{24}(\bar{W})-\tilde{L}_{25}(\bar{N}^T)=-\frac{1}{2}\tilde{L}(\bar{W}+2\bar{W}^*,\bar{W}) \quad (2)$$

$$\tilde{L}_{31}(\bar{W})+\tilde{L}_{32}(\bar{\Psi}_x)-\tilde{L}_{33}(\bar{\Psi}_y)+\tilde{L}_{34}(\bar{F})-\tilde{L}_{35}(\bar{N}^T)-\tilde{L}_{36}(\bar{S}^T)=0 \quad (3)$$

$$\tilde{L}_{41}(\bar{W})-\tilde{L}_{42}(\bar{\Psi}_x)+\tilde{L}_{43}(\bar{\Psi}_y)+\tilde{L}_{44}(\bar{F})-\tilde{L}_{45}(\bar{N}^T)-\tilde{L}_{46}(\bar{S}^T)=0 \quad (4)$$

where $\tilde{L}(\ )$ is the nonlinear operator concerning the geometric nonlinearity in the von Kármán sense and $\tilde{L}_{ij}(\ )$ are the linear operators. The details of these operators are given in Shen (2009a).

In the above equations, $\bar{N}^T$, $\bar{M}^T$, $\bar{S}^T$ and $\bar{P}^T$ are the forces, moments and higher order moments caused by elevated temperature, and are defined by

$$\begin{bmatrix}\bar{N}_x^T\\ \bar{N}_y^T\\ \bar{N}_{xy}^T\end{bmatrix}\begin{bmatrix}\bar{M}_x^T\\ \bar{M}_y^T\\ \bar{M}_{xy}^T\end{bmatrix}\begin{bmatrix}\bar{P}_x^T\\ \bar{P}_y^T\\ \bar{P}_{xy}^T\end{bmatrix}=\sum_{k=1}\int_{t_{k-1}}^{t_k}\begin{bmatrix}A_x\\ A_y\\ A_{xy}\end{bmatrix}_k(1,Z,Z^3)\Delta T\,dZ \quad (5a)$$

$$\begin{bmatrix}\bar{S}_x^T\\ \bar{S}_y^T\\ \bar{S}_{xy}^T\end{bmatrix}=\begin{bmatrix}\bar{M}_x^T\\ \bar{M}_y^T\\ \bar{M}_{xy}^T\end{bmatrix}-\frac{4}{3t^2}\begin{bmatrix}\bar{P}_x^T\\ \bar{P}_y^T\\ \bar{P}_{xy}^T\end{bmatrix} \quad (5b)$$

where $\Delta T=T-T_0$ is temperature rise from some reference temperature T_0 at which there are no thermal strains, and

$$\begin{bmatrix}A_x\\ A_y\\ A_{xy}\end{bmatrix}=-\begin{bmatrix}\bar{Q}_{11}&\bar{Q}_{12}&\bar{Q}_{16}\\ \bar{Q}_{12}&\bar{Q}_{22}&\bar{Q}_{26}\\ \bar{Q}_{16}&\bar{Q}_{26}&\bar{Q}_{66}\end{bmatrix}\begin{bmatrix}1&0\\ 0&1\\ 0&0\end{bmatrix}\begin{bmatrix}\alpha_{11}\\ \alpha_{22}\end{bmatrix} \quad (6)$$

where α_{11} and α_{22} are the thermal expansion coefficients measured in the X and Y directions for the$k$th ply, and $\bar{Q}_{ij}$ are the transformed elastic constants with details being given in Reddy (1984a; 1984b). Note that for an FG-CNTRC layer, $\bar{Q}_{ij}=Q_{ij}$ in which

$$Q_{11}=\frac{E_{11}}{1-\nu_{12}\nu_{21}},\quad Q_{22}=\frac{E_{22}}{1-\nu_{12}\nu_{21}},\quad Q_{12}=\frac{\nu_{21}E_{11}}{1-\nu_{12}\nu_{21}},$$
$$Q_{16}=Q_{26}=0,\quad Q_{66}=G_{12} \quad (7)$$

where E_{11}, E_{22}, G_{12}, ν_{12} and ν_{21} are the effective Young's and shear moduli and Poisson's ratio of the FG-CNTRC layer, respectively.

The effective material properties of the FG-CNTRCs plates are derived from the corresponding properties of the CNTs and the matrix by the use of a micromechanical model as follows [Shen (2009b)]

$$E_{11} = \eta_1 V_{CN} E_{11}^{CN} + V_m E^m \tag{8a}$$

$$\frac{\eta_2}{E_{22}} = \frac{V_{CN}}{E_{22}^{CN}} + \frac{V_m}{E^m} \tag{8b}$$

$$\frac{\eta_3}{G_{12}} = \frac{V_{CN}}{G_{12}^{CN}} + \frac{V_m}{G^m} \tag{8c}$$

where E_{11}^{CN}, E_{22}^{CN} and G_{12}^{CN} are the Young's and shear moduli of the CNTs, E^m and G^m are the corresponding properties for the matrix, and the $\eta_j(j$=1,2,3) are the CNT efficiency parameters, respectively. In addition,V_{CN} and V_m are the volume fractions of the CNT and the matrix, which satisfy the relationship of $V_{CN} + V_m$ = 1.

The CNT efficiency parameters η_j in Eq. (8) is introduced to account for the size dependent material properties of CNTs resulting from the fact that the load transfer between the nanotube and polymeric phases is less than perfect, for instance, the surface effect, strain gradient effect, intermolecular coupled stress effect. The values of η_j will be determined later by matching the elastic moduli of FG-CNTRCs predicted by the MD simulations with the prediction of the extended rule of mixture in Eq. (8).

To avoid abrupt changes of the material properties, we assume only linear distribution that can readily be achieved in practice, such as,

$$V_{CN} = 2\left(\frac{t_1 - Z}{t_1 - t_0}\right) V_{CN}^* \text{ (for the top layer)} \tag{9a}$$

$$V_{CN} = 2\left(\frac{Z - t_1}{t_2 - t_1}\right) V_{CN}^* \text{ (for the bottom layer)} \tag{9b}$$

in which

$$V_{CN}^* = \frac{w_{CN}}{w_{CN} + (\rho_{CN}/\rho_m) - (\rho_{CN}/\rho_m) w_{CN}} \tag{9c}$$

where w_{CN} is the mass fraction of nanotube, and ρ_{CN} and ρ_m are the densities of the carbon nanotube and the matrix, respectively. It is evident that when $Z = t_0$(top surface) and $Z = t_2$(bottom surface) $V_{CN} = 2V_{CN}^*$, and when $Z = t_1$ (middle surface) V_{CN}=0. In such a way, the two cases of uniformly distributed (UD), i.e. $V_{CN} = V_{CN}^*$, and functionally graded (FG) CNTRCs will have the same value of mass fraction of nanotube.

In Eq. (6), the thermal expansion coefficients in the longitudinal and transverse directions can be expressed as

$$\alpha_{11} = V_{CN}\alpha_{11}^{CN} + V_m\alpha^m \tag{10a}$$

$$\alpha_{22} = (1+\nu_{12}^{CN})V_{CN}\alpha_{22}^{f} + (1+\nu^m)V_m\alpha^m - \nu_{12}\alpha_{11} \tag{10b}$$

where α_{11}^{CN}, α_{22}^{CN} and α^m are the thermal expansion coefficients, and ν_{12}^{CN} and ν^m are the Poisson's ratios of the carbon nanotube and the matrix, respectively. Note that α_{11} and α_{22} are also graded linearly in the Z direction.

Furthermore, we assume that the material properties of the CNTs and the matrix are temperature dependant. Thus, the effective material properties of FG-CNTRCs, such as Young's modulus, shear modulus and thermal expansion coefficients, are functions of temperature and position. Accordingly, the effective Poisson's ratio depends weakly on temperature change and position [Morimoto et al. (2003)] and is expressed as

$$\nu_{12} = V_{CN}^{*}\nu_{12}^{CN} + V_m\nu^m \tag{11}$$

We assume all edges of the FG-CNTRC plate are simply supported. Depending upon the in-plane behavior at the edges, two cases, Case 1 (referred to herein as movable edges) and Case 2 (referred to herein as immovable edges), will be considered, such that

Case 1: The edges are simply supported and freely movable in the in-plane directions. In addition the plate is subjected to uniaxial compressive edge loads.

Case 2: All four edges are simply supported. Uniaxial edge loads are applied in the X-direction. The edges at X= 0 and a are considered freely movable (in the in-plane direction) while the remaining two edges being unloaded and immovable (i.e. prevented from moving in the Y-direction).

For both cases, the associated boundary conditions can be expressed as

X = 0, a:

$$\bar{W} = \bar{\Psi}_y = 0 \tag{12a}$$

$$\bar{N}_{xy} = 0, \quad \bar{M}_x = \bar{P}_x = 0 \tag{12b}$$

$$\int_0^b \bar{N}_x\, dY + P = 0 \tag{12c}$$

Y = 0, b:

$$\bar{W} = \bar{\Psi}_x = 0 \tag{12d}$$

$$\bar{N}_{xy} = 0, \quad \bar{M}_y = \bar{P}_y = 0 \tag{12e}$$

$$\int_0^a \bar{N}_y \, dX = 0 \text{ (movable edges)} \tag{12f}$$

$$\bar{V} = 0 \text{ (immovable edges)} \tag{12g}$$

where P is a compressive edge load in the X-direction, $\bar{M}_x$ and $\bar{M}_y$ are the bending moments and $\bar{P}_x$ and $\bar{P}_y$ are the higher order moments as defined in Reddy (1984a; 1984b).

The condition of the immovable condition, $\bar{V}$= 0 at Y= 0 and b is satisfied on the average sense as

$$\int_0^a \int_0^b \frac{\partial \bar{V}}{\partial Y} dY dX = 0 \tag{13}$$

This condition in conjunction with Eq. (14b) below leads to compressive stresses acting on the edges at Y = 0 and b. The accuracy and effectiveness of Eq. (13) for the buckling analysis of plates have been shown in Shen and Zhang (1988) and Librescu et al. (1995).

Finally, we need to establish the postbuckling load-shortening relationships of the plate for the postbuckling analysis. The averaged end-shortening relationships are defined as

$$\begin{aligned}
\frac{\Delta_x}{a} &= -\frac{1}{ab} \int_0^b \int_0^a \frac{\partial \bar{U}}{\partial X} dX dY \\
&= -\frac{1}{ab} \int_0^b \int_0^a \left\{ \left[A_{11}^* \frac{\partial^2 \bar{F}}{\partial Y^2} + A_{12}^* \frac{\partial^2 \bar{F}}{\partial X^2} + \left(B_{11}^* - \frac{4}{3t^2} E_{11}^* \right) \frac{\partial \bar{\Psi}_x}{\partial X} + \left(B_{12}^* - \frac{4}{3t^2} E_{12}^* \right) \frac{\partial \bar{\Psi}_y}{\partial Y} \right. \right. \\
&\quad \left. - \frac{4}{3t^2} \left(E_{11}^* \frac{\partial^2 \bar{W}}{\partial X^2} + E_{12}^* \frac{\partial^2 \bar{W}}{\partial Y^2} \right) \right] \\
&\quad \left. - \frac{1}{2} \left(\frac{\partial \bar{W}}{\partial X} \right)^2 - \frac{\partial \bar{W}}{\partial X} \frac{\partial \bar{W}^*}{\partial X} - (A_{11}^* \bar{N}_x^T + A_{12}^* \bar{N}_y^T) \right\} dX dY
\end{aligned} \tag{14a}$$

$$\frac{\Delta_y}{b} = -\frac{1}{ab}\int_0^a\int_0^b \frac{\partial \bar{V}}{\partial Y}dYdY$$

$$= -\frac{1}{ab}\int_0^a\int_0^b \left\{\left[A_{22}^*\frac{\partial^2 \bar{F}}{\partial X^2} + A_{12}^*\frac{\partial^2 \bar{F}}{\partial Y^2} + \left(B_{21}^* - \frac{4}{3t^2}E_{21}^*\right)\frac{\partial \bar{\Psi}_x}{\partial X} + \left(B_{22}^* - \frac{4}{3t^2}E_{22}^*\right)\frac{\partial \bar{\Psi}_y}{\partial Y}\right.\right.$$

$$\left. - \frac{4}{3t^2}\left(E_{21}^*\frac{\partial^2 \bar{W}}{\partial X^2} + E_{22}^*\frac{\partial^2 \bar{W}}{\partial Y^2}\right)\right]$$

$$\left. -\frac{1}{2}\left(\frac{\partial \bar{W}}{\partial Y}\right)^2 - \frac{\partial \bar{W}}{\partial Y}\frac{\partial \bar{W}^*}{\partial Y} - (A_{12}^*\bar{N}_x^T + A_{22}^*\bar{N}_y^T)\right\}dYdX \quad (14b)$$

where Δ_x and Δ_y are the averaged end-shortening displacements of the plate in the X and Y directions, and for the case of immovable unloaded edges Δ_y must be zero-valued.

In the above equations, the reduced stiffness matrices $[A_{ij}^*]$, $[B_{ij}^*]$, $[D_{ij}^*]$, $[E_{ij}^*]$, $[F_{ij}^*]$ and $[H_{ij}^*]$ are functions of temperature T and spatial position Z in the thickness direction, determined through relationships [Shen (2009a)]

$$\begin{aligned}&\mathbf{A}^* = \mathbf{A}^{-1}, \quad \mathbf{B}^* = -\mathbf{A}^{-1}\mathbf{B}, \quad \mathbf{D}^* = \mathbf{D} - \mathbf{B}\mathbf{A}^{-1}\mathbf{B}, \quad \mathbf{E}^* = -\mathbf{A}^{-1}\mathbf{E},\\ &\mathbf{F}^* = \mathbf{F} - \mathbf{E}\mathbf{A}^{-1}\mathbf{B}, \quad \mathbf{H}^* = \mathbf{H} - \mathbf{E}\mathbf{A}^{-1}\mathbf{E}\end{aligned} \quad (15)$$

where A_{ij}, B_{ij} etc., are the plate stiffnesses, defined by

$$(A_{ij}, B_{ij}, D_{ij}, E_{ij}, F_{ij}, H_{ij}) = \sum_{k=1}^{} \int_{t_{k-1}}^{t_k} (Q_{ij})_k (1, Z, Z^2, Z^3, Z^4, Z^6)dZ \quad (i, j = 1, 2, 6) \quad (16a)$$

$$(A_{ij}, D_{ij}, F_{ij}) = \sum_{k=1}^{} \int_{t_{k-1}}^{t_k} (Q_{ij})_k (1, Z^2, Z^4)dZ \quad (i, j = 4, 5) \quad (16b)$$

3 Solution methodology

A two-step perturbation technique is employed to determine the buckling loads and postbuckling equilibrium paths of CNTRC plates in this section. Before carrying out the solution process, it is convenient first to define the following dimensionless quantities

$$x = \pi\frac{X}{a}, \quad y = \pi\frac{Y}{b}, \quad \beta = \frac{a}{b},$$

$$(W,W^*)=\frac{(\bar{W},\bar{W}^*)}{[D_{11}^*D_{22}^*A_{11}^*A_{22}^*]^{1/4}},\quad F=\frac{\bar{F}}{[D_{11}^*D_{22}^*]^{1/2}},$$

$$(\Psi_x,\Psi_y)=\frac{a}{\pi}\frac{(\bar{\Psi}_x,\bar{\Psi}_y)}{[D_{11}^*D_{22}^*A_{11}^*A_{22}^*]^{1/4}},\quad \gamma_{14}=\left[\frac{D_{22}^*}{D_{11}^*}\right]^{1/2},$$

$$\gamma_{24}=\left[\frac{A_{11}^*}{A_{22}^*}\right]^{1/2},\quad \gamma_5=-\frac{A_{12}^*}{A_{22}^*},\quad (\gamma_{T1},\gamma_{T2})=\frac{a^2}{\pi^2}\frac{(A_x^T,A_y^T)}{[D_{11}^*D_{22}^*]^{1/2}},$$

$$(M_x,\ P_x)=\frac{a^2}{\pi^2}\frac{1}{D_{11}^*[D_{11}^*D_{22}^*A_{11}^*A_{22}^*]^{1/4}}\left(\bar{M}_x,\ \frac{4}{3t^2}\bar{P}_x\right),$$

$$(\delta_x,\delta_y)=\left(\frac{\Delta_x}{a},\frac{\Delta_y}{b}\right)\frac{b^2}{4\pi^2[D_{11}^*D_{22}^*A_{11}^*A_{22}^*]^{1/2}},\quad \lambda_x=\frac{Pb}{4\pi^2\ [D_{11}^*D_{22}^*]^{1/2}} \tag{17}$$

in which A_x^T and A_y^T are defined by

$$\begin{bmatrix}A_x^T\\A_y^T\end{bmatrix}\Delta T=-\sum_{k=1}\int_{t_{k-1}}^{t_k}\begin{bmatrix}A_x\\A_y\end{bmatrix}_k\Delta T\,dZ \tag{18}$$

and the details of which can be found in Appendix A of Shen and Zhang (2010).

Substituting Eq. (17) into the nonlinear Eqs. (1)-(4) leads to a simple form as

$$L_{11}(W)-L_{12}(\Psi_x)-L_{13}(\Psi_y)=\gamma_{14}\beta^2L(W+W^*,F) \tag{19}$$

$$L_{21}(F)=-\frac{1}{2}\gamma_{24}\beta^2L(W+2W^*,W) \tag{20}$$

$$L_{31}(W)+L_{32}(\Psi_x)-L_{33}(\Psi_y)=0 \tag{21}$$

$$L_{41}(W)-L_{42}(\Psi_x)+L_{43}(\Psi_y)=0 \tag{22}$$

where all dimensionless linear operators $L_{ij}(\ )$ and nonlinear operator$L(\ )$ are defined as in Shen (2009a).

The boundary conditions expressed by Eq. (12) can also expressed in dimensionless forms as

$x = 0, \pi$:

$$W=\Psi_y=0 \tag{23a}$$

$$F_{,xy}=M_x=P_x=0 \tag{23b}$$

$$\frac{1}{\pi}\int_0^{\pi}\beta^2\frac{\partial^2F}{\partial y^2}dy+4\lambda_x\beta^2=0 \tag{23c}$$

$y = 0, \pi$:

$$W = \Psi_x = 0 \tag{23d}$$

$$F_{,xy} = M_y = P_y = 0 \tag{23e}$$

$$\int_0^{\pi} \frac{\partial^2 F}{\partial x^2} dx = 0 \text{ (movable edges)} \tag{23f}$$

$$\delta_y = 0 \text{ (immovable edges)} \tag{23g}$$

and the dimensionless end-shortening relationships become

$$\delta_x = -\frac{1}{4\pi^2\beta^2\gamma_{24}} \int_0^{\pi}\int_0^{\pi} \left\{ \left[\gamma_{24}^2 \beta^2 \frac{\partial^2 F}{\partial y^2} - \gamma_5 \frac{\partial^2 F}{\partial x^2} \right] - \frac{1}{2}\gamma_{24} \left(\frac{\partial W}{\partial x} \right)^2 - \gamma_{24} \frac{\partial W}{\partial x} \frac{\partial W^*}{\partial x} \right.$$

$$\left. + (\gamma_{24}^2 \gamma_{T1} - \gamma_5 \gamma_{T2}) \Delta T \right\} dxdy \tag{24a}$$

$$\delta_y = -\frac{1}{4\pi^2\beta^2\gamma_{24}} \int_0^{\pi}\int_0^{\pi} \left\{ \left[\frac{\partial^2 F}{\partial x^2} - \gamma_5 \beta^2 \frac{\partial^2 F}{\partial y^2} \right] - \frac{1}{2}\gamma_{24}\beta^2 \left(\frac{\partial W}{\partial y} \right)^2 - \gamma_{24}\beta^2 \frac{\partial W}{\partial y} \frac{\partial W^*}{\partial y} \right.$$

$$\left. + (\gamma_{T2} - \gamma_5 \gamma_{T1}) \Delta T \right\} dydx \tag{24b}$$

It should be noted that the thermal coupling in Eqs. (1)-(4) vanishes because the temperature rise ΔT is assumed to be uniform, but the term ΔT intervenes in Eq. (24).

Now one is in a position to solve Eqs. (19)-(22) with boundary conditions (23). We assume that

$$W(x,y,\varepsilon) = \sum_{j=1} \varepsilon^j w_j(x,y), \quad F(x,y,\varepsilon) = \sum_{j=0} \varepsilon^j f_j(x,y),$$

$$\Psi_x(x,y,\varepsilon) = \sum_{j=1} \varepsilon^j \psi_{xj}(x,y), \quad \Psi_y(x,y,\varepsilon) = \sum_{j=1} \varepsilon^j \psi_{yj}(x,y) \tag{25}$$

where ε is a small perturbation parameter, for which we do not give a real physical meaning at the first step.

Substituting Eq. (25) into Eqs. (19)-(22) and comparing the power of ε, we derive a set of perturbation equations, such that,

$$O(\varepsilon^1): \quad L_{11}(w_1) - L_{12}(\psi_{x1}) - L_{13}(\psi_{y1}) = \gamma_{14}\beta^2 L(w_1 + W^*, f_0) \tag{26a}$$

$$L_{21}(f_1) = 0 \tag{26b}$$

$$L_{31}(w_1)+L_{32}(\psi_{x1})-L_{33}(\psi_{y1})=0 \tag{26c}$$

$$L_{41}(w_1)-L_{42}(\psi_{x1})+L_{43}(\psi_{y1})=0 \tag{26d}$$

$$O(\varepsilon^2): \quad L_{11}(w_2)-L_{12}(\psi_{x2})-L_{13}(\psi_{y2})=\gamma_{14}\beta^2[L(w_2,f_0)+L(w_1+W^*,f_1)] \tag{27a}$$

$$L_{21}(f_2)=-\frac{1}{2}\gamma_{24}\beta^2 L(w_1+2W^*,w_1) \tag{27b}$$

$$L_{31}(w_2)+L_{32}(\psi_{x2})-L_{33}(\psi_{y2})=0 \tag{27c}$$

$$L_{41}(w_2)-L_{42}(\psi_{x2})+L_{43}(\psi_{y2})=0 \tag{27d}$$

Assume the first term of $w_j\ (x,y)$ has the form of classical buckling mode of plate, such as,

$$w_1(x,y)=A_{11}^{(1)}\sin mx\sin ny \tag{28}$$

and the initial geometric imperfection has a similar form

$$W^*(x,y,\varepsilon)=\varepsilon a_{11}^*\sin mx\sin ny=\varepsilon\mu A_{11}^{(1)}\sin mx\sin ny \tag{29}$$

where $\mu=a_{11}^*/A_{11}^{(1)}$ is the imperfection parameter.

By using Eqs. (28) and (29) to solve these perturbation equations of each order, the amplitudes of the terms $w_j(x,y)$, $f_j(x,y)$, $\psi_{xj}(x,y)$ and $\psi_{yj}(x,y)$ are determined step by step. Substituting these solved functions back into Eq. (25), we obtain the asymptotic solutions of the deflection, stress function and rotations of the plate up to the 4^{th} order, such that

$$W=\varepsilon[A_{11}^{(1)}\sin mx\sin ny]+\varepsilon^3[A_{13}^{(3)}\sin mx\sin 3ny+A_{31}^{(3)}\sin 3mx\sin ny]+O(\varepsilon^5) \tag{30}$$

$$\begin{aligned}F=&-B_{00}^{(0)}\frac{y^2}{2}-b_{00}^{(0)}\frac{x^2}{2}+\varepsilon^2[-B_{00}^{(2)}\frac{y^2}{2}-b_{00}^{(2)}\frac{x^2}{2}+B_{20}^{(2)}\cos 2mx+B_{02}^{(2)}\cos 2ny]\\&+\varepsilon^4[-B_{00}^{(4)}\frac{y^2}{2}-b_{00}^{(4)}\frac{x^2}{2}+B_{20}^{(4)}\cos 2mx+B_{02}^{(4)}\cos 2ny+B_{22}^{(4)}\cos 2mx\cos 2ny\\&+B_{40}^{(4)}\cos 4mx+B_{04}^{(4)}\cos 4ny+B_{24}^{(4)}\cos 2mx\cos 4ny+B_{42}^{(4)}\cos 4mx\cos 2ny]\\&+O(\varepsilon^5)\end{aligned} \tag{31}$$

$$\Psi_x=\varepsilon[C_{11}^{(1)}\cos mx\sin ny]+\varepsilon^3[C_{13}^{(3)}\cos mx\sin 3ny+C_{31}^{(3)}\cos 3mx\sin ny]+O(\varepsilon^5)$$

(32)

$$\Psi_y = \varepsilon[D_{11}^{(1)} \sin mx \cos ny] + \varepsilon^3[D_{13}^{(3)} \sin mx \cos 3ny + D_{31}^{(3)} \sin 3mx \cos ny] + O(\varepsilon^5) \tag{33}$$

Note that all coefficients in Eqs. (30)-(33) are related and can be expressed in terms of $A_{11}^{(1)}$. The detailed expressions of the coefficients are not shown here for the sake of brevity.

After solving the displacement, stress, and rotation, we can solve the postbuckling equilibrium path. Substituting Eqs. (30)-(33) into the boundary conditions (23c) and (24a), the postbuckling equilibrium path can be written as

$$\lambda_x = \lambda^{(0)} + \lambda^{(2)}(A_{11}^{(1)}\varepsilon)^2 + \lambda^{(4)}(A_{11}^{(1)}\varepsilon)^4 + \cdots \tag{34}$$

and

$$\delta_x = \delta^{(0)} + \delta^{(2)}(A_{11}^{(1)}\varepsilon)^2 + \delta^{(4)}(A_{11}^{(1)}\varepsilon)^4 + \cdots \tag{35}$$

In Eqs. (34) and (35), $(A_{11}^{(1)}\varepsilon)$ is taken as the second perturbation parameter relating to the dimensionless maximum deflection W_m. From Eq. (30), taking $(x,y) = (\pi/2m, \pi/2n)$ yields

$$A_{11}^{(1)}\varepsilon = W_m + \Theta_1 W_m^2 + \cdots \tag{36}$$

Eqs. (34) and (35) may then be re-written as

$$\lambda_x = \lambda_x^{(0)} + \lambda_x^{(2)} W_m^2 + \lambda_x^{(4)} W_m^4 + \ldots \tag{37}$$

and

$$\delta_x = \delta_x^{(0)} + \delta_x^{(2)} W_m^2 + \delta_x^{(4)} W_m^4 + \ldots \tag{38}$$

It is noted that $\lambda_x^{(i)}$ and $\delta_x^{(i)}$ (i= 0,2,4,...) are related to the material properties and are all functions of temperature T and position Z, and the details of which may be found in Shen (2009a).

The perturbation scheme described presented here is quite different from the traditional one by Chia (1980), where the small perturbation parameter is defined by normalizing the maximum central deflection of the plate $\bar{W}_m$ by the plate thickness

t, such as, $\varepsilon = \bar{W}_m/t$. Generally, we need $\varepsilon < 1$ in the regular perturbation technique. It is worth noting that ε is no longer a small perturbation parameter in the deep postbuckling region when the plate deflection is sufficiently large, i.e. $\bar{W}_m/t > 1$, and in such a case the solution may be invalid. Contrast to the tradition perturbation scheme, the present work avoids the paradox by a two step perturbation scheme where ε is definitely a small perturbation parameter in the first step and $(A_{11}^{(1)}\varepsilon)$ in the second step may be large in the large deflection region.

Eqs. (37) and (38) can be employed to obtain numerical results for the postbuckling load-deflection and load-end-shortening curves of simply supported FG-CNTRC plates subjected to uniaxial compression in thermal environments. The buckling load of a perfect plate can readily be obtained by settingμ= 0 (or $\bar{W}^*/t = 0$), while taking W_m = 0 (or $\bar{W}/t$= 0). In the present case, the minimum load (called buckling load) and corresponding buckling mode (m,n) can be determined by comparing the axial loads [obtained from Eq. (37)] under various values of (m,n) that determine the number of half-waves in the X and Y directions.

4 Numerical results and discussions

Numerical results are presented in this section for perfect and imperfect, geometrically mid-plane symmetric FG-CNTRC plates subjected to uniaxial compression. Firstly, we need to determine the effective material properties of CNTRCs. The matrix is assumed to be made of Poly (methyl methacrylate), referred to as PMMA, and its material properties are assumed to be ν^m=0.34, $\alpha^m = 45(1+0.0005\Delta T) \times 10^{-6}$/K and E^m= (3.52-0.0034T) GPa, in which T = T_0 +ΔT andT_0 = 300K (room temperature). In such a way, α^m= 45.0$\times 10^{-6}$/K and E^m=2.5 GPa at T=300 K. The (10,10) SWCNTs are selected as reinforcements. Han and Elliott (2007) chose E_{11}^{CN}=600 GPa, E_{22}^{CN}=10 GPa, G_{12}^{CN}=17.2 GPa and ν_{12}^{CN}=0.19 for (10,10) SWCNTs. Such a low value of Young's modulus is due to the fact that the effective thickness of CNTs is assumed to be 0.34 nm or more. However, as reported recently the effective thickness of SWCNTs should be smaller than 0.142 nm [Wang and Zhang (2008)]. Therefore, all material properties and effective thickness of SWCNTs used for analysis will be re-examined and properly chosen in the present paper by MD simulations.

The MD simulations were carried out to solve the Newtonian equations of motion governed by interatomic interactions numerically to determine the trajectories of a large number of atoms. A Velocity-Verlet algorithm was used to integrate the equations of motion with a basic time step of 0.5 fs to guarantee a good conservation of energy. The interaction between carbon atoms was modeled by the many-body reactive empirical bond order potential developed by Brenner et al. (2002) while the

long-range van der Waals interaction between CNTs was described by the Lennard-Jones 12-6 potentials [Girifalco and Lad (1956)]. System temperature conversion was carried out by the Nose-Hoover feedback thermostat [Hoover (1985)]. To begin the MD simulation, the CNT was initially optimized and freely relaxed to reach the minimum energy configuration. The deformation of the CNT was carried out in a quasi-static way by gradually increasing the applied load in a small increment and allowing the tube to relax fully until the next equilibrium configuration was reached. The perfect CNTs subjected to axial compression and torsion were simulated under temperature varying from 300 K to 1000 K. Fixed boundary condition was assumed to be at one end of the tube, and axial compressive force P or torque M_s was applied on the other end with the appropriate constraints. From MD simulations, the material properties and effective wall thickness for armchair (10, 10) SWCNT were determined uniquely and typical results are listed in Tab. 1 [Shen and Zhang (2010)]. These results confirm that the material properties of CNTs are size-dependent [Elliott et al. (2004); Jin and Yuan (2003); Chang et al. (2005); Wang et al. (2005)] and temperature-dependent [Zhang and Shen (2006a); Zhang and Shen (2006b)]. It is noted that the effective wall thickness obtained for (10,10)-tube is h=0.067 nm, which satisfies the Vodenitcharova-Zhang criterion [Wang and Zhang (2008)], and the wide used value of 0.34 nm for tube wall thickness is thoroughly inappropriate for SWCNTs.

Table 1: Temperature-dependent material properties for (10,10) SWCNT (L=9.26 nm, R =0.68 nm, h=0.067 nm, ν_{12}^{CN}=0.175) [from Shen and Zhang (2010)]

Temperature (K)	E_{11}^{CN} (TPa)	E_{22}^{CN} (TPa)	G_{12}^{CN} (TPa)	α_{11}^{CN} ($\times 10^{-6}$/K)	α_{22}^{CN} ($\times 10^{-6}$/K)
300	5.6466	7.0800	1.9445	3.4584	5.1682
500	5.5308	6.9348	1.9643	4.5361	5.0189
700	5.4744	6.8641	1.9644	4.6677	4.8943

The key issue for successful application of the extended rule of mixture to CNTRCs is to determine the CNT efficiency parameter η_j (j=1, 2, 3). For short fiber composites η_1 is usually taken to be 0.2 [Fukuda and Kawata (1974)]. However, there are no experiments conducted to determine the value of η_j for CNTRCs. For the current analysis, the CNT efficiency parameters η_1, η_2 and η_3 are determined by matching the Young's moduli E_{11} and E_{22} and shear modulusG_{12} of CNTRCs predicted from the extended rule of mixture to those from the MD simulations given by Han and Elliott (2007) and Griebel and Hamaekers (2004). Typical results are listed in Tab. 2 and will be used in all the following examples, in which taking η_3:η_2= 0.7: 1 and $G_{13} = G_{12}$ andG_{23}=1.2G_{12} [Song and Youn (2006)].

Table 2: Comparisons of elastic moduli for Polymer/CNT composites reinforced by (10,10)-tube under T=300K [from Shen and Zhang (2010)].

V^*_{CN}	MD [Griebel and Hamaekers (2004)][a]			Rule of mixture					
	E_{11} (GPa)	E_{22} (GPa)	G_{12} (GPa)	E_{11} (GPa)	η_1	E_{22} (GPa)	η_2	G_{12} (GPa)	η_3
0.028	1.74	0.81	0.19	1.74	0.0058	0.81	0.931	0.19	0.642
	MD [Han and Elliott (2007)][b]			Rule of mixture					
0.12	94.6	2.9	–	94.78	0.137	2.9	1.022	–	–
0.17	138.9	4.9	–	138.68	0.142	4.9	1.626	–	–
0.28	224.2	5.5	–	224.50	0.141	5.5	1.585	–	–

[a] E^m=0.85 GPa, ν^m=0.44; [b] E^m=2.5 GPa, ν^m=0.34

The accuracy and effectiveness of the present method for buckling and postbuckling analyses of isotropic and orthotropic plates subjected to uniaxial and/or biaxial compression, excluding temperature effects, were examined by many comparison studies given in Shen (2000a; 2000b; 2005). For instance, the postbuckling load–deflection curves for perfect and imperfect, isotropic thin square plates (ν= 0.326) subjected to uniaxial compression were compared with the analytical solutions of Dym (1974) and the experimental results of Yamaki (1961); and the postbuckling load–deflection curves of a transversely isotropic square thick plate (b/t =10) with its longitudinal edges immovable subjected to uniaxial compression were compared with the higher order shear deformation theory (HSDPT) solutions of Librescu and Stein (1991); and the postbuckling load–deflection curves of single-ply orthotropic square thick plate (b/t =10) subjected to equal biaxial compression were compared with HSDPT results given by Bhimaraddi (1992). These comparisons show that the solutions from present method are in good agreement with existing results.

Once the material properties of SWCNTs are properly determined, a parametric study are carried out and their results are shown in Tabs. 3 and 4, and Figs. 2-6. For these examples, the width-to-thickness ratios of the plate are chosen as b/t= 20 and 100, and the thickness of each FGM layer is taken to be 1.0 mm. A double-thickness uniformly distributed (UD) CNTRC plate is also considered as a comparator. The total thickness of these two types of CNTRC plates is the same, i.e. t= 2.0 mm. It should be noted that in all figures $\bar{W}^*/t$ denotes the dimensionless maximum initial geometric imperfection of the plate.

Table 3 presents the buckling loads P_{cr}(in kN) for perfect, shear deformable (b/t=20),

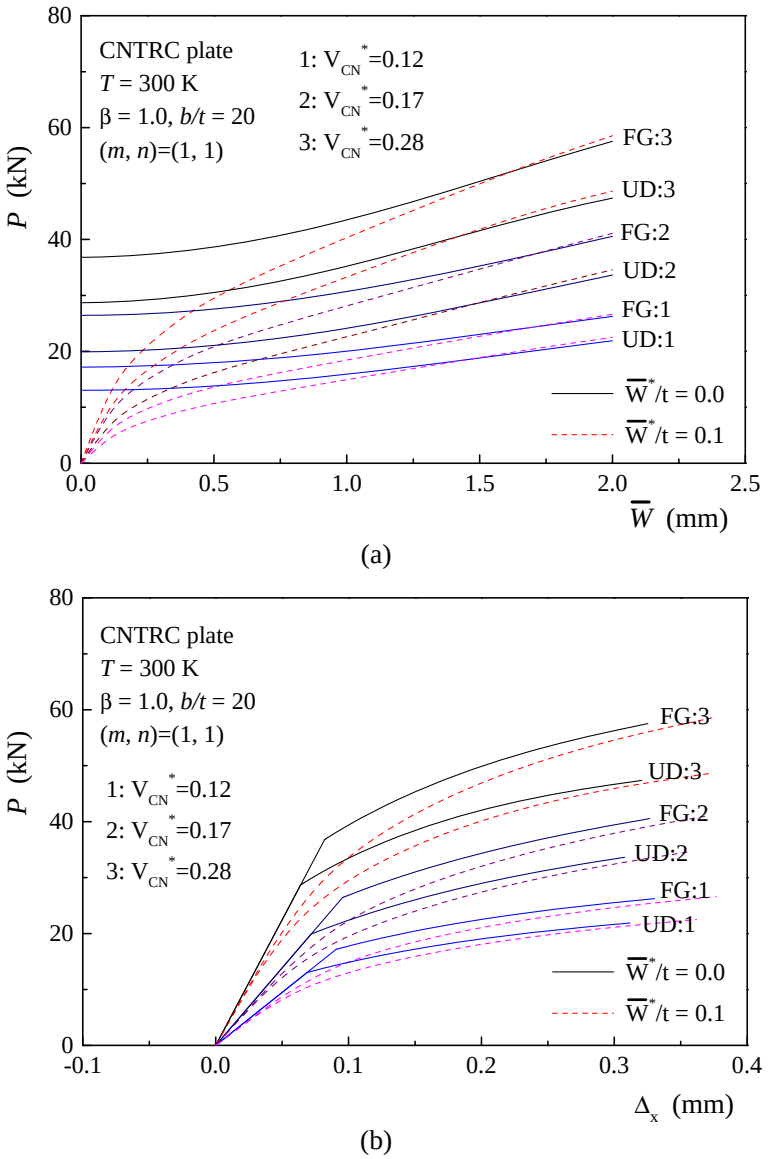

Figure 2: Effect of nanotube volume fraction on the postbuckling behavior of CNTRC plates: (a) load-deflection; (b) load-shortening.

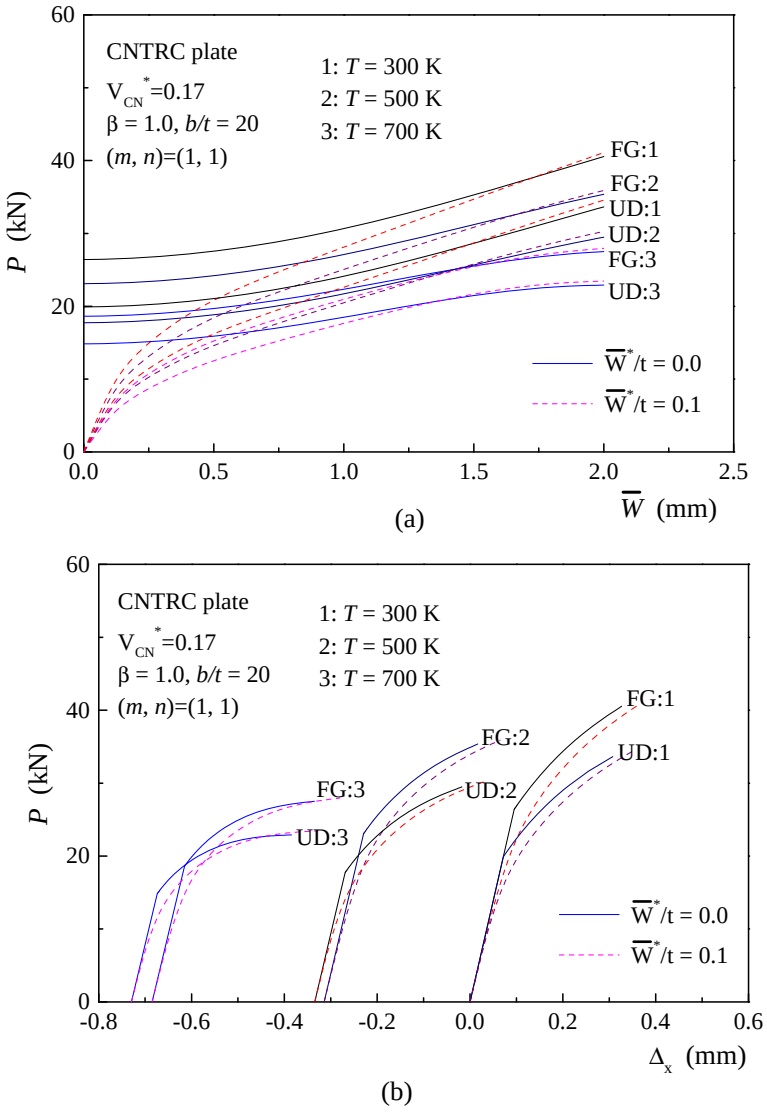

Figure 3: Effect of temperature changes on the postbuckling behavior of CNTRC plates: (a) load-deflection; (b) load-shortening.

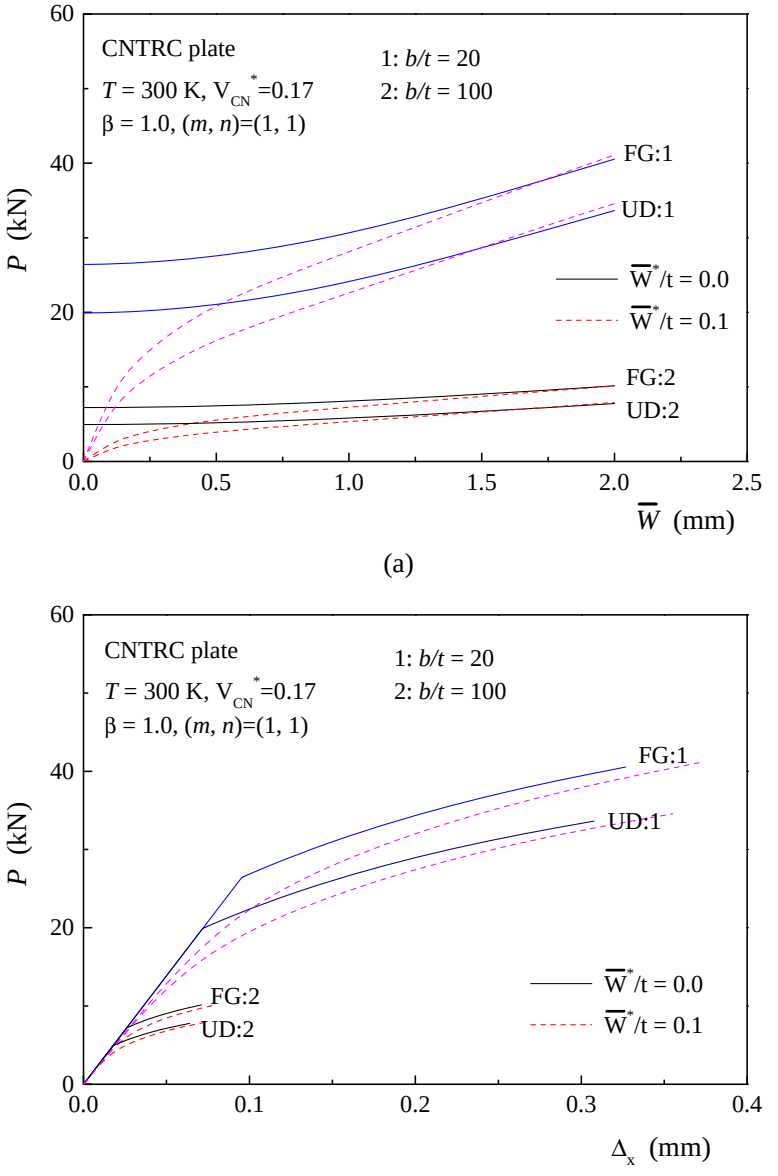

Figure 4: Effect of plate thickness ratio b/t on the postbuckling behavior of CNTRC plates: (a) load-deflection; (b) load-shortening.

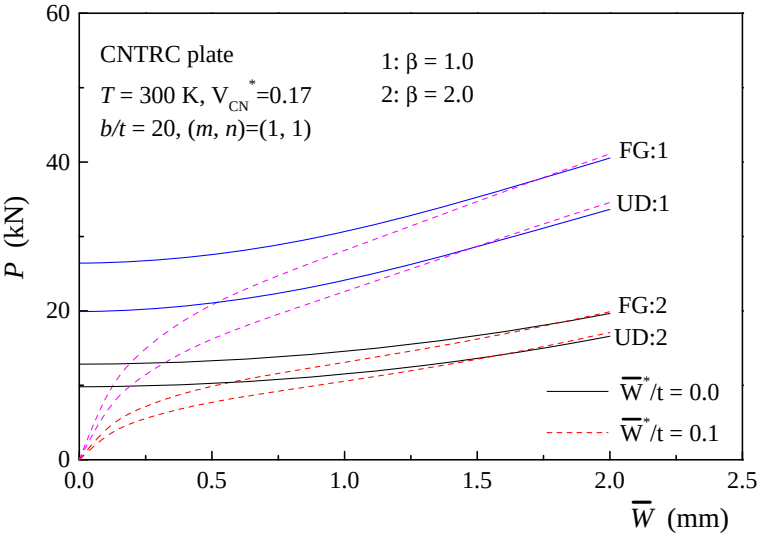

(a)

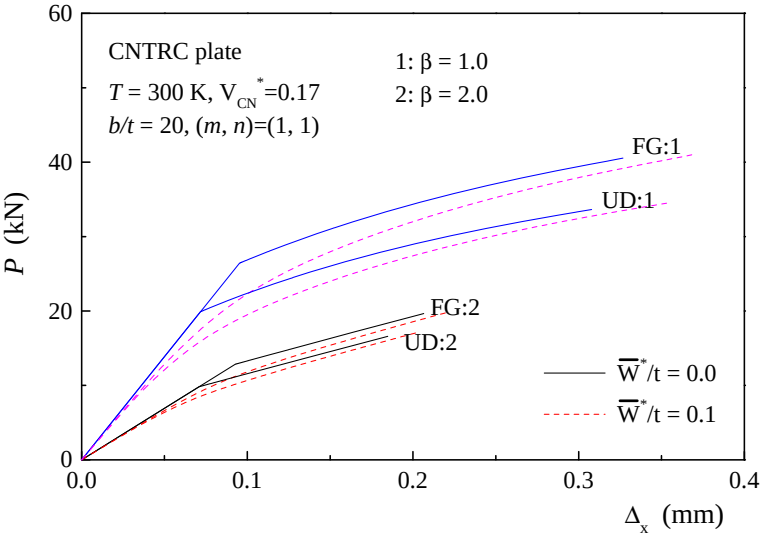

(b)

Figure 5: Effect of plate aspect ratio on the postbuckling behavior of CNTRC plates: (a) load-deflection; (b) load-shortening.

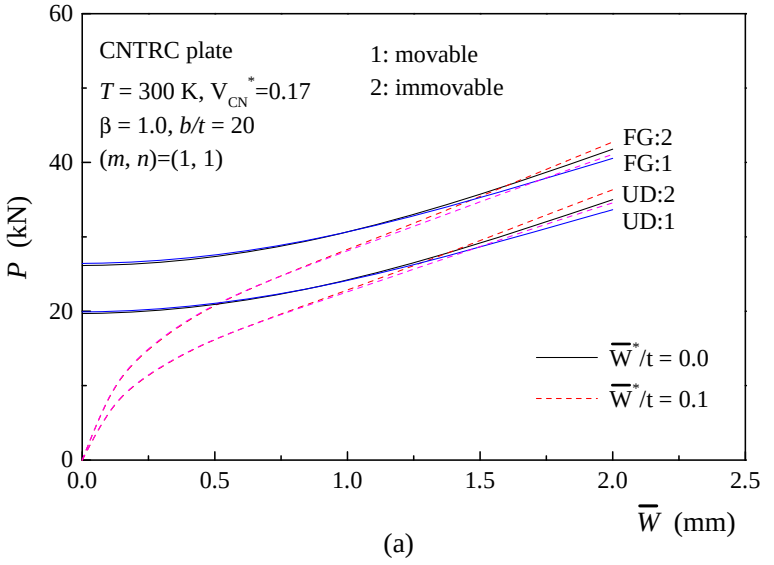

(a)

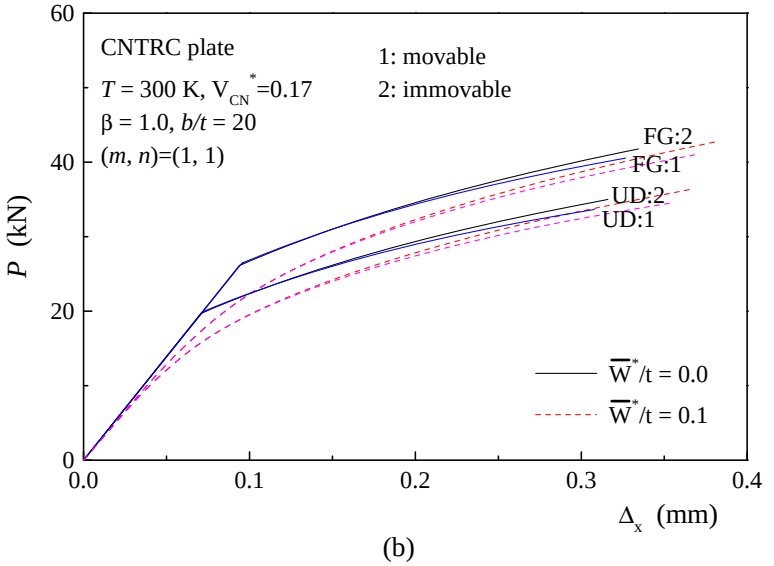

(b)

Figure 6: Comparisons of postbuckling behavior of a CNTRC plate under two cases of in-plane boundary conditions: (a) load-deflection; (b) load-shortening.

Table 3: Comparisons of buckling loads P_{cr} (in kN) for perfect, moderately thick, CNTRC plates under thermal environments (a/b=1.0, b/t= 20, t=2 mm).

thermal	$V^*_{CN}=0.12$		$V^*_{CN}=0.17$		$V^*_{CN}=0.28$	
environments	UD	FG	UD	FG	UD	FG
unloaded edges movable						
300 K	13.04	17.18(+32%)[a]	19.91	26.42(+33%)	28.69	36.78(+28%)
500 K	11.54	14.93(+29%)	17.74	23.10(+30%)	25.22	31.45(+25%)
700 K	9.54	11.92(+25%)	14.84	18.63(+26%)	20.51	24.39(+19%)
unloaded edges immovable						
300 K	12.91	17.01(+32%)	19.70	26.13(+33%)	28.48	36.51(+28%)
500 K	9.95	13.31(+34%)	15.16	20.47(+35%)	22.63	28.80(+27%)
700 K	4.95[b]	7.52[b](+52%)	7.75[b]	12.12[b](+56%)	13.95[b]	19.25[b](+38%)

[a] Difference=100%[P_{cr}(FG)-P_{cr}(UD)]/P_{cr}(UD);

[b] buckling mode (m, n)=(1, 2), otherwise (m, n)=(1, 1).

Table 4: Comparisons of buckling loads P_{cr} (in kN) for perfect, thin, CNTRC plates under thermal environments [b/t= 100, t=2 mm, (m, n)=(1, 1)].

thermal	$V^*_{CN}=0.12$		$V^*_{CN}=0.17$		$V^*_{CN}=0.28$	
environment	UD	FG	UD	FG	UD	FG
Square plate (a/b=1.0)						
300 K	3.34	4.87(+46%)[a]	4.96	7.23(+46%)	7.76	11.41(+47%)
500 K	3.18	4.64(+46%)	4.71	6.90(+46%)	7.43	10.92(+47%)
700 K	3.03	4.44(+47%)	4.49	6.59(+47%)	7.12	10.44(+47%)
Rectangular plate (a/b=2.0)						
300 K	1.32	1.77(+34%)	2.06	2.76(+34%)	2.86	4.06(+42%)
500 K	1.15	1.57(+36%)	1.78	2.43(+36%)	2.54	3.64(+43%)
700 K	0.99	1.38(+39%)	1.51	2.11(+40%)	2.23	3.23(+45%)

[a] Difference=100%[P_{cr}(FG)-P_{cr}(UD)]/P_{cr}(UD);

CNTRC plates with three different values of the CNT volume fraction V^*_{CN} (=0.12, 0.17 and 0.28) subjected to uniaxial compression under three thermal environmental conditions (T= 300, 500 and 700K). Correspondingly, the CNT mass fractions are w_{CN}= 0.142, 0.2 and 0.321, respectively, by taking the density of carbon nanotube ρ_{CN}=1.4 g/cm^3 and the density of matrix ρ_m=1.15 g/cm^3 in Eq. (9c). Two types of the in-plane boundary conditions are considered. For most cases, the buckling mode is found to be (m,n)=(1, 1) and (m,n)=(1, 2) for the plate with immovable unloaded edges under T=700K. Here, UD represents uniformly distributed

CNTRC plates and FG represents functionally graded CNTRC plates. It can be found that the buckling load of CNTRC plates, both UD and FG, is lower in case of immovable unloaded edges than movable edges. It can also be found that the buckling load of FG-CNTRC plate is higher than that of the UD-CNTRC plate. The percentage of increase is about 19% to 35% for the plate with (m,n)=(1, 1) and is about 38% to 56% for the plate with (m,n)=(1, 2), as shown in the brackets. Furthermore, the buckling loads increase as CNT volume fraction V_{CN}^{*} increases, but decrease as temperature increases. The percentage of decrease is about 29% for the FG-CNTRC plate with movable edges and about 54% for the same plate with immovable unloaded edges when the temperature changes from T=300 K to T= 700 K under the same CNT volume fraction V_{CN}^{*}=0.17.

Table 4 gives the buckling loads P_{cr}(in kN) for perfect, thin (b/t=100) CNTRC plates with three different values of the CNT volume fraction V_{CN}^{*} under the same loading conditions as mentioned before. Now two cases of the plate aspect ratio $\beta = a/b$=1.0 and 2.0 are considered. It is found that both square and rectangular plates have the same buckling mode (m,n)=(1, 1), and the buckling loads of rectangular plates are much lower than those of the square plates under the same CNT volume fraction and thermal environmental condition.

In the following, the postbuckling load-deflection and load-shortening curves for imperfect FG- and UD-CNTRC plates have been shown, along with the perfect plate results, in Figs. 2-6. It is worth noting that the mode of postbuckling deformation is unchanged, i.e. (m, n) = (1, 1), although mode changes are possible in the deep postbuckling range, i.e. secondary buckling phenomena in reality and the whole postbuckling equilibrium path can easily be obtained by increasing the number of half-waves in the X direction [Shen and Zhang (1988)]. Such buckling mode changes are, however, not considered in the present study.

Fig. 2 shows the effect of the CNT volume fraction V_{CN}^{*} (=0.12, 0.17 and 0.28) on the postbuckling behavior of FG- and UD-CNTRC plates subjected to uniaxial compression at T= 300 K. It can be seen that the increase of the CNT volume fraction V_{CN}^{*} yields an increase of the buckling load and postbuckling strength as well as the stiffness of the plate. The buckling load as well as postbuckling strength of FG-CNTRC plate is much greater than that of UD-CNTRC plate. The postbuckling equilibrium paths for both FG- and UD-CNTRC plates are stable, and both plates are insensitive to initial geometric imperfection.

Fig. 3 shows the effect of the temperature changes on the postbuckling behavior of FG- and UD-CNTRC plates with V_{CN}^{*}=0.17 subjected to uniaxial compression. Since the material properties for both matrix and SWCNTs are assumed to be temperature-dependent, the increase in temperature reduces the elastic moduli and degrades the strength of the CNTRC plates. It can be seen that both buckling load

and postbuckling strength are decreased with the temperature increase, and both FG- and UD-CNTRC plates become softer when T= 700 K.

Fig. 4 shows the effect of plate width-to-thickness ratio b/t(= 20 and 100) on the postbuckling behavior of FG- and UD-CNTRC plates with V_{CN}^{*}=0.17 subjected to uniaxial compression at$T$= 300 K. It can be seen that the buckling load and postbuckling strength of a shear deformable plate (b/t =20) are considerably greater than those of the thin plate (b/t =100). The difference between two postbuckling curves of FG- and UD-CNTRC plates is more pronounced in case of b/t =20 than b/t=100.

Fig. 5 shows the effect of plate aspect ratio β(=1.0 and 2.0) on the postbuckling behavior of FG- and UD-CNTRC plates with V_{CN}^{*}=0.17 subjected to uniaxial compression at$T$= 300 K. As expected, the buckling load and postbuckling strength decreases as the plate aspect ratioβ increases.

Fig. 6 shows the effect of in-plane boundary conditions on the postbuckling behavior of FG- and UD-CNTRC plates with V_{CN}^{*}=0.17 subjected to uniaxial compression at$T$= 300 K. The load-deflection and load-shortening curves of FG- and UD-CNTRC square plates under 'movable' and 'immovable' in-plane boundary conditions are displayed. The results show that the plate with movable edges has a higher buckling load but lower postbuckling strength when $\bar{W}/t$>0.5.

Finally, Figs. 2-6 show that the deflections of an imperfect plate deviate greatly from those of a perfect plate, and therefore, the bifurcation buckling do not exist even though the configuration of the plate is mid-plane symmetric.

5 Concluding remarks

Postbuckling behavior of nanocomposite plates with functionally graded nanotube reinforcements subjected to uniaxial compression in thermal environments has been presented. Micromechanical model and multi-scale approach are used to derive the effective material properties of the CNTRC plates. The scale effect of CNT reinforcements is considered by introducing the CNT efficiency parameter that is estimated by matching the elastic modulus of CNTRCs predicted by the MD simulations with the prediction of the extended rule of mixture. A parametric study for geometrically mid-plane symmetric FG- and UD- CNTRC plates with low CNT volume fractions has been carried out. The results obtained demonstrate that the linear functionally graded nano-reinforcement has a quantitative effect on the buckling load as well as postbuckling strength of the plates. In addition, the postbuckling behaviors of CNTRC plates are also significantly influenced by temperature rise, the transverse shear deformation, the plate aspect ratio as well as the CNT volume fraction. However, the effect of in-plane boundary conditions on the postbucking

strength of the CNTRC plates is relative small.

References

Bhimaraddi, A. (1992): Buckling and post-buckling behavior of laminated plates using the generalized nonlinear formulation. *Int. J. Mech. Sci.* vol. 34, pp. 703-715.

Birman, V. (1995): Stability of functionally graded hybrid composite plates. *Composites Engineering*, vol. 5, pp. 913-921.

Brenner, D.W.; Shenderova, O.A.; Harrison, J.A.; Stuart, S.J.; Ni, B.; Sinnott, S.B. (2002): A second-generation reactive empirical bond order (REBO) potential energy expression for hydrocarbons. *J. Phys. Condens. Matter*, vol. 14, pp. 783-802.

Carrera, E. (2003): Historical review of Zig-Zag theories for multilayered plates and shells. *Appl. Mech. Rev.*, vol. 56, pp. 287-308.

Chang, T.; Geng, J.; Guo, X. (2005): Chirality- and size-dependent elastic properties of single-walled carbon nanotubes. *Appl. Phys. Lett.*, vol. 87, pp. 251929.

Chia, C.Y. (1980): *Nonlinear Analysis of Plates*. McGraw-Hill.

Dym, C.L. (1974): *Stability Theory and Its Applications to Structural Mechanics*. Noordhoff, Leyden.

Elliott, J.A.; Sandler, J.K.W.; Windle, A.H.; Young, R.J.; Shaffer, M.S.P. (2004): Collapse of single-wall carbon nanotubes is diameter dependent. *Phys. Rev. Lett.*, vol. 92, pp. 095501.

Endo, M.; Hayashi, T.; Kim, Y.A.; Terrones, M.; Dresselhaus, M.S. (2004): Applications of carbon nanotubes in the twenty–first century. *Philos. T. R. Soc. A.*, vol. 362, pp. 2223-2238.

Esawi, A.M.K.; Farag, M.M. (2007): Carbon nanotube reinforced composites: Potential and current challenges. *Mater. Des.*, vol. 28, pp. 2394-2401.

Feldman, E.; Aboudi, J. (1997): Buckling analysis of functionally graded plates subjected to uniaxial loading. *Compos. Struct.*, vol. 38, pp. 29-36.

Fidelus, J.D.; Wiesel, E.; Gojny, F.H.; Schulte, K.; Wagner, H.D. (2005): Thermo-mechanical properties of randomly oriented carbon/epoxy nanocomposites. *Composites A*, vol. 36, pp. 1555-1561.

Formica, G.; Lacarbonara, W.; Alessi, R. (2010): Vibrations of carbon nanotube-reinforced composites. *J. Sound Vib.*, vol. 329, pp. 1875-1889.

Fukuda, H.; Kawata, K. (1974): On Young's modulus of short fibre composites. *Fibre Sci. Technol.*, vol. 7, pp. 207-222.

Girifalco, L.A.; Lad, R.A. (1956): Energy of cohesion, compressibility, and the potential energy functions of the graphite system. *J. Chem. Phys.*, vol. 25, pp. 693–697.

Griebel, M.; Hamaekers, J. (2004): Molecular dynamics simulations of the elastic moduli of polymer–carbon nanotube composites. *Comput. Methods Appl. Mech. Eng.*, vol. 193, pp. 1773–1788.

Han, Y.; Elliott, J. (2007): Molecular dynamics simulations of the elastic properties of polymer/carbon nanotube composites. *Comput. Mater. Sci.*, vol. 39, pp. 315-323.

Hoover, W.G. (1985): Canonical dynamics: Equilibrium phase-space distributions. *Phys. Rev. A*, vol. 31, pp. 1695-1697.

Jin, Y.; Yuan, F.G. (2003): Simulation of elastic properties of single-walled carbon nanotubes. *Compos. Sci. Technol.*, vol. 63, pp. 1507-1515.

Ke, L.-L.; Yang, J.; Kitipornchai, S. (2010): Nonlinear free vibration of functionally graded carbon nanotube-reinforced composite beams. *Compos. Struct.*, vol. 92, pp. 676-683.

Li, X.; Gao, H.; Scrivens, W.A.; Fei, D.; Xu, X.; Sutton, M.A.; Reynolds, A.P.; Myrick, M.L. (2007): Reinforcing mechanisms of single-walled carbon nanotube-reinforced polymer composites. *J. Nanosci. Nanotechnol.*, vol. 7, pp. 2309–2317.

Librescu, L.; Lin, W.; Nemeth, M.P.; Starnes, J.H. (1995): Thermomechanical postbuckling of geometrically imperfect flat and curved panels taking into account tangential edge constraints. *J. Thermal Stresses*, vol. 18, pp. 465-482.

Librescu, L.; Stein, M. (1991): A geometrically nonlinear theory of transversely isotropic laminated composite plates and its use in the post-buckling analysis, *Thin-Walled Struct.*, vol. 11, pp. 177-201.

McClory, C.; Chin, S.J.; McNally, T. (2009): Polymer/carbon nanotube composites. *Aust. J. Chem.*, vol. 62, pp. 762–785.

Meguid, S.A.; Sun, Y. (2004): On the tensile and shear strength of nano-reinforced composite interfaces. *Mater. Des*. vol. 25, pp. 289-296.

Morimoto, T.; Tanigawa, Y.; Kawamura, R. (2003): Thermal buckling analysis of inhomogeneous rectangular plate due to uniform heat supply. *J. Thermal Stresses*, vol. 26, pp. 1151–1170.

Navazi, H.M.; Haddadpour, H. (2008): Nonlinear cylindrical bending analysis of shear deformable functionally graded plates under different loadings using analytical methods. *Int. J. Mech. Sci.*, vol. 50, pp. 1650-1657.

Qian, D.; Dickey, E.C.; Andrews, R.; Rantell, T. (2000): Load transfer and deformation mechanisms in carbon nanotube-polystyrene composites. *Appl. Phys.*

Lett., vol. 76, pp. 2868–2870.

Reddy, J.N. (1984a): A simple higher-order theory for laminated composite plates. *J. Appl. Mech.*, vol. 51, pp. 745-752.

Reddy, J.N. (1984b): A refined nonlinear theory of plates with transverse shear deformation. *Int. J. Solids Struct.*, vol. 20, pp. 881-896.

Schadler, L.S.; Giannaris, S.C.; Ajayan, P.M. (1998): Load transfer in carbon nanotube epoxy composites. *Appl. Phys. Lett.*, vol. 73, pp. 3842–3844.

Seidel, G.D.; Lagoudas, D.C. (2006): Micromechanical analysis of the effective elastic properties of carbon nanotube reinforced composites. *Mech. Mater.*, vol. 38, pp. 884-907.

Shen, H.-S. (2000a): Thermomechanical postbuckling of imperfect shear deformable laminated plates on elastic foundations. *Comput. Methods Appl. Mech. Eng.*, vol. 189, pp. 761–784.

Shen, H.-S. (2000b): Postbuckling of shear deformable laminated plates under biaxial compression and lateral pressure and resting on elastic foundations. *Int. J. Mech. Sci.*, vol. 42, pp. 1171–1195.

Shen, H.-S. (2005): Postbuckling of FGM plates with piezoelectric actuators under thermo-electro-mechanical loadings. *Int. J. Solids Struct.*, vol. 42, pp. 6101-6121.

Shen, H.-S. (2009a): *Functionally Graded Materials Nonlinear Analysis of Plates and Shells*. Boca Raton: CRC Press.

Shen, H.-S. (2009b): Nonlinear bending of functionally graded carbon nanotube-reinforced composite plates in thermal environments. *Compos. Struct.*, vol. 91, pp. 9-19.

Shen, H.-S.; Zhang, C.-L. (2010): Thermal buckling and postbuckling behavior of functionally graded carbon nanotube-reinforced composite plates. *Mater. Des.*, vol. 31, pp. 3403–3411.

Shen, H.-S.; Zhang, J.W. (1988): Perturbation analyses for the postbuckling of simply supported rectangular plates under uniaxial compression. *Appl. Math. Mech.*, vol. 9, pp. 793-804.

Song, Y.S.; Youn, J.R. (2006): Modeling of effective elastic properties for polymer based carbon nanotube composites. *Polymer*, vol. 47, pp. 1741–1748.

Thostenson, E.T.; Ren, Z.; Chou, T.-W. (2010): Advances in the science and technology of carbon nanotubes and their composites: a review. *Compos. Sci. Technol.*, vol. 61, pp. 1899-1912.

Tsai, J.-L.; Tzeng, S.-H.; Chiu, Y.-T. (2010): Characterizing elastic properties of carbon nanotubes/polyimide nanocomposites using multi-scale simulation. *Com-*

posites B, vol. 41, pp. 106-115.

Vodenitcharova, T.; Zhang, L.C. (2006): Bending and local buckling of a nanocomposite beam reinforced by a single-walled carbon nanotube. *Int. J. Solids Struct.*, vol. 43, pp. 3006-3024.

Wang, C.Y.; Zhang, L.C. (2008): A critical assessment of the elastic properties and effective wall thickness of single-walled carbon nanotubes. *Nanotechnology*, vol. 19, pp. 075705.

Wang, L.; Zheng, Q.; Liu, J.Z.; Jinag, Q. (2005): Size dependence of the thin-shell model for carbon nanotubes. *Phys. Rev. Lett.* vol. 95, pp. 105501.

Woo, J.; Meguid, S.A.; Stranart, J.C.; Liew, K.M. (2005): Thermomechanical postbuckling analysis of moderately thick functionally graded plates and shallow shells. *Int. J. Mech. Sci.*, vol. 47, pp. 1147-1171.

Wuite, J.; Adali, S. (2005): Deflection and stress behaviour of nanocomposite reinforced beams using a multiscale analysis. *Compos. Struct.*, vol. 71, pp. 388–396.

Yamaki, N. (1961): Experiments on the postbuckling behavior of square plates loaded in edge compression. *J. Appl. Mech. ASME*, vol. 28, pp. 238–244.

Yang, J.; Liew, K.M.; Kitipornchai, S. (2006): Imperfection sensitivity of the post-buckling behavior of higher-order shear deformable functionally graded plates. *Int. J. Solids Struct.*, vol. 43, pp. 5247-5266.

Yas, M.H.; Aragh, B.S. (2010): Three-dimensional analysis for thermoelastic response of functionally graded fiber reinforced cylindrical panel. *Compos. Struct.*, vol. 92, pp. 2391–2399.

Zhang, C.-L.; Shen, H.-S. (2006a): Buckling and postbuckling analysis of single-walled carbon nanotubes in thermal environments via molecular dynamics simulation. *Carbon*, vol. 44, pp. 2608-2616.

Zhang, C.-L.; Shen, H.-S. (2006b): Temperature-dependent elastic properties of single-walled carbon nanotubes: Prediction from molecular dynamics simulation. *Appl. Phys. Lett.*, vol. 89, pp. 081904.

Zhu, R.; Pan, E.; Roy, A.K. (2007): Molecular dynamics study of the stress–strain behavior of carbon-nanotube reinforced Epon 862 composites. *Mater. Sci. Eng. A*, vol. 447, pp. 51-57.